ARTICLE

Ag or Au Nanoparticle-Embedded One-Dimensional Composite TiO_2 Nanofibers Prepared via Electrospinning for Use in Lithium-Ion Batteries

Sang Hoon Nam,[†] Hee-Sang Shim,[‡] Youn-Su Kim,[§] Mushtaq Ahmad Dar,[†] Jong Guk Kim,[†] and Won Bae Kim*,[†]

Department of Materials Science and Engineering and Research Institute for Solar & Sustainable Energies (RISE), Gwangju Institute of Science and Technology (GIST), 261 Chemdan-gwagiro, Buk-gu, Gwangju 500-712, South Korea, and Department of Mechanical Engineering, Stevens Institute of Technology, Castle Point on Hudson, Hoboken, New Jersey 07030

ABSTRACT We prepared metallic-nanoparticle-embedded one-dimensional titanium dioxide (1D-TiO_2) via a one-step electrospinning process, in which Au or Ag metallic nanoparticles between 5 and 10 nm in diameter were incorporated within the TiO_2 nanofibers. After calcination of the composite nanofibers at high temperature of 450 °C, the nanofibers were converted to 1D-TiO_2 by the thermal decomposition of polyvinylpyrrolidone (PVP). This process simultaneously changed the metal precursors ($AgNO_3$ or $HAuCl_4 \cdot 3H_2O$) to metallic nanoparticles (Ag or Au) to produce 1D-TiO_2 nanofiber composites (Ag@1D-TiO_2 or Au@1D-TiO_2). The influences of Ag or Au incorporation into the 1D-TiO_2 nanofibers were studied using various microscopic and X-ray spectroscopic methods. Because of the changes in crystallinity and size of TiO_2 in the Ag@1D-TiO_2 and Au@1D-TiO_2 nanostructures, lithium-ion diffusion and charge transfer were promoted. In particular, in comparison to pristine 1D-TiO_2, the specific capacity of metal nanoparticle-embedded 1D-TiO_2 nanofiber composites was increased by at least 20%, and the rate performance was improved 2-fold. Consequently, we propose that these metal-nanoparticle-embedded 1D-nanostructures prepared via electrospinning may be useful as electrodes in lithium-ion batteries.

KEYWORDS: titanium dioxide • nanofiber • nanoparticle • electrospinning • lithium-ion battery • anode • X-ray absorption

INTRODUCTION

Titanium dioxide (TiO_2) is a widely used material in both research and industrial fields due to its inherent chemical stability, transparency, low cost, and minimal toxicity. However, the specific tailoring of the physicochemical properties of TiO_2 still offers a great deal of room for investigation. In the case of lithium-ion (Li-ion) storage, TiO_2 is a promising anode material in terms of safety because it alleviates the overcharge problem by moving toward a higher potential, thereby avoiding the lithium plating and the parasitic electrochemical reaction (1).

In previous work, several factors affecting the lithium storage properties of TiO_2 were reported (2–4). Size optimization of TiO_2 nanoparticles is necessary for good electrochemical performance. The nanoparticle size can be controlled in a certain range by varying the templates (5), surfactant (6), and temperature (7). In general, small TiO_2 nanoparticles show a superior capacity during initial stages, but they have disadvantages such as fast decay of capacity (8). Another important consideration in the use of TiO_2 is its polymorphism. Titanium ions in the anatase structure are arranged in a tetragonal configuration with [TiO_6] octahedral units including two axial Ti−O bonds, which are slightly longer than four equatorial Ti−O bonds. The distortion of the [TiO_6] octahedral unit is greater in the anatase than in the rutile phase (9), but it is smaller than in brookite (10). For Li-ion storage, the anatase TiO_2 phase is favorable because Li-ions readily penetrate into the structure and exhibits thermodynamic stability (11). Recently, 1D TiO_2 (1D-TiO_2) nanostructures have begun to attract increased attention for Li-ion storage as compared to bulk TiO_2 materials because of their enlarged surface areas and their reduced diffusion lengths. Several synthetic methodologies for the construction of 1D TiO_2 nanostructures in the form of nanowires (12), nanorods (13), and nanotubes (14) have been reported. However, the electrical conductivity still needs to be improved for achieving full electrode utilization, sufficient battery power, and fast discharge/charge rates (15–17).

It has been shown that the incorporation of metal nanoparticles in Li-ion batteries can improve the electrical conductivity of electrodes through the formation of a conductive percolation network (18–20). Metal-embedded electrodes

* Corresponding author. E-mail: wbkim@gist.ac.kr. Tel: 82-62-715-2317. Fax: 82-62-715-2304.

Received for review April 9, 2010 and accepted June 28, 2010

[†] Department of Materials Science and Engineering, Gwangju Institute of Science and Technology.

[‡] Research Institute for Solar & Sustainable Energies (RISE), Gwangju Institute of Science and Technology.

[§] Stevens Institute of Technology.

DOI: 10.1021/am100319u

2010 American Chemical Society

Published on Web 07/08/2010

usually increase the specific capacity by about 10−30% as compared to electrodes without metal particles. In this study, we prepared an anatase 1D TiO_2 that was composited with metal nanoparticles such as Ag or Au (Ag@1D-TiO_2 or Au@1D-TiO_2) in a one-step manner using electrospinning method, which is known as useful preparation tool for inorganic 1D nanostructure fabrications (21–23). Electrospinning offers a versatile method to produce various binary or multicomponent 1D nanocomposites via sol−gel processes. By altering the composition of the electrospinning solution that contains two or more soluble precursors, a variety of 1D composite nanofibers can be readily fabricated. In this work, we chose an Ag or Au-embedded TiO_2 nanofiber system because we hope that embedded Ag or Au might maintain its nanoparticle morphology inside of the electrochemically active TiO_2 matrix, thereby the metal nanoparticles are constructed within 1D TiO_2 nanostructures to give the better electrical conductivity. Various microscopic, X-ray spectroscopic, and electrochemical characterizations were performed to verify the enhanced Li-ion storage performance of Ag@1D-TiO_2 and Au@1D-TiO_2.

EXPERIMENTAL SECTION

The electrospinning solution was prepared as follows: Tetrabutyl orthotitanate (Aldrich, 97%, 1.5 g), acetic acid (1 mL), and ethanol (1 mL) were vigorously mixed using a magnetic stirrer for 1 h. Silver nitrate ($AgNO_3$, Aldrich) or chloroauric acid ($HAuCl_4 \cdot 3H_2O$, Aldrich) was dissolved in ethanol, and polyvinylpyrrolidone (PVP; M_w = 1 300 000 g mol^{-1}, Aldrich) was subsequently added to the solution. The prepared solutions were then mixed using a magnetic stirrer for 30 min. The resulting electrospinning solutions appeared transparent with a slight yellowish color, indicating that the sol−gel reaction was properly achieved. For metallic nanoparticle incorporation, $AgNO_3$ (0.035 g) or $HAuCl_4 \cdot 3H_2O$ (0.042 g) was added to the electrospinning solutions, and the solutions were then instantly loaded into a syringe with a 23-gauge stainless steel needle. At this point, an electric field potential of 10 kV was applied between the needle tip and a grounded substrate at a distance of 8 cm. The collected electrospun nanofibers were similar in appearance to a web and were detached from the substrate. Finally, after a heat treatment at 500 °C for 3 h in air, reflective bluish Ag- or Au-embedded TiO_2 nanofibers (Ag@1D-TiO_2 or Ag@1D-TiO_2) were obtained.

The structural properties of the prepared samples were characterized by field emission scanning electron microscopy (FESEM; JEOL S7600), high-resolution transmission electron microscopy (HRTEM; JEOL F20), X-ray diffraction (Rigaku X-ray diffractometer), and X-ray absorption fine structure (XAFS). X-ray absorption measurements were conducted on 3C1 EXAFS and 7C EC beamlines (Pohang Accelerator Laboratory; 2.5 GeV, Korea). The spectra were measured at room temperature in the transmission mode for the K-edge of Ti (4966 eV) under the ambient condition. Energy calibration was conducted using a standard Ti foil. Higher-order harmonic oscillations were avoided by detuning the monochromator to decrease the incident X-ray intensity by approximately 30%. The X-ray absorption near-edge spectra were analyzed using IFEFFIT (24, 25). The extended X-ray absorption fine structure (EXAFS) data were analyzed using IFEFFIT (24, 25) and FEFF 8.4 code (26). For Fourier transformation, k_{min} and k_{max} were selected in the range of 2.5 and 12.0 $Å^{-1}$ for TiO_2 EXAFS, respectively. The k^3-weighted EXAFS function was applied for Fourier transformation, in which the signals without Fourier filtering were converted in R space over the region of 1.0 to 3.0 Å. The theoretical standard functions for Ti−O and Ti−Ti single scattering were synthesized with the FEFF code using structural information for an anatase TiO_2 material (27).

The electrochemical experiments were performed using two-electrode systems. The prepared samples were used as the working electrodes and metallic lithium was used as the counter electrode. The two-electrode systems were assembled into a cell in an argon circulating glovebox for electrochemical measurements. A 1 M $LiPF_6$ solution in a 1:1 mixture of ethylene carbonate and diethyl carbonate was used as the electrolyte. The cell was tested in the galvanostatic discharge/charge mode with a voltage window of 3.0 to 1.0 V (vs Li/Li^+) at a constant current using a cycler (WonA tech, WBCS3000, Korea). Cyclic voltammetry was performed over a potential range of 3.0 to 1.0 V at various scan rates of 0.1, 0.25, 0.5, 1, and 2 mVs^{-1} using a Solartron 1470E multistat system. AC impedance data were collected by a Solartron 1260 frequency response analyzer. Amplitude voltage of 10 mV was applied over the frequency ranges from 250 kHz to 10 mHz.

RESULTS AND DISCUSSION

Figure 1 shows the morphologies of the 1D-TiO_2, Ag@1D-TiO_2, and Au@1D-TiO_2 samples prepared by the electrospinning process with subsequent heat treatment. Scanning electron microscopy (SEM) and transmission electron microscopy (TEM) images indicate that all of the nanofibers were continuous 1D structures formed through the calcination process, although the metal nanoparticles were loaded at the amount of 10 wt % in the nanofibers. As shown in Figure 1a−c, only small differences were observed between the pristine 1D-TiO_2 and the metal-embedded TiO_2, as projected on the surface of the nanofiber composites. The average diameter of the nanofibers was 50 ± 20 nm. Further investigation using TEM images (Figure 1d−f) showed that these nanofibers were indeed individual 1D structure, and the incorporated nanoparticles could be distinguished from the nanofibers by showing sharp contrast. The incorporated nanoparticles were mostly spherical in shape and embedded throughout the whole 1D-TiO_2 host matrix. The surface morphologies of Ag@1D-TiO_2 and Au@1D-TiO_2 were relatively smooth, whereas the pristine 1D-TiO_2 seemed to consist of continuous nanoparticles having diameters of 5−10 nm and a rough surface. These nanoparticle characteristics suggest that the Ag or Au is well-dispersed within the TiO_2 nanofibers. The selective area electron diffraction (SAED) shown in Figure 1g−i indicates a diffuse ring pattern, implying the existence of polycrystalline properties. The Ag@1D-TiO_2 shown in Figure 1h displayed a broader line profile than the pristine 1D-TiO_2. In contrast, the Au@1D-TiO_2 in Figure 1 exhibited small and bright spot patterns on the diffuse ring. These results indicate that the Au nanoparticles in the Au@1D-TiO_2 might influence the growth orientation of TiO_2 through interaction effects (28). The Au(111) plane is parallel to the TiO_2(112) plane in the anatase phase. The nanostructural features of TiO_2 surrounded with Au nanoparticles were also changed in the surface region of the TEM results (data not shown). To the best of our knowledge, an orientation relationship between Ag and TiO_2 has not been reported. However, such a change of crystallinity in

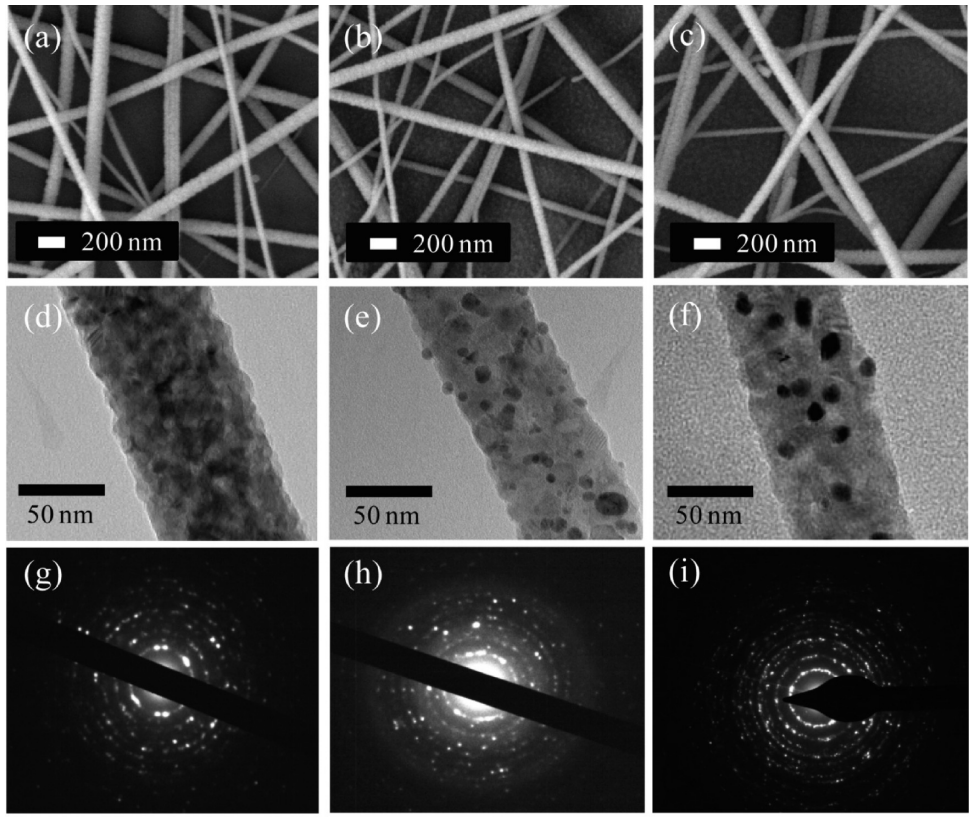

FIGURE 1. FESEM images of (a) pristine 1D-TiO_2, (b) Ag@1D-TiO_2, and (c) Au@1D-TiO_2 after calcination; TEM images of (d) pristine 1D-TiO_2, (e) Ag@1D-TiO_2, and (f) Au@1D-TiO_2. (g–i) SEAD patterns on the location of d–f.

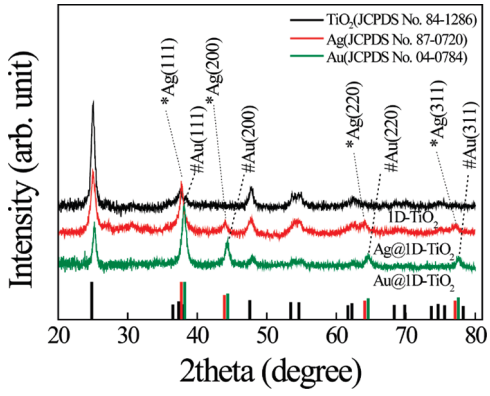

FIGURE 2. X-ray diffraction patterns of 1D-TiO_2, Ag@1D-TiO_2, and Au@1D-TiO_2. All diffraction peaks can be indexed to those of the anatase phase of TiO_2, Ag, and Au.

metal-incorporated TiO_2 can affect the Li-ion storage performance by changing the scattering path of the electrons (29).

To analyze the crystallographic structures of the Ti, Ag, and Au states in the prepared samples, X-ray diffraction (XRD) was employed. As shown in Figure 2, all scattered XRD peaks were identical to the standard peaks of TiO_2, Ag, and Au, implying that the precursors were successfully converted to TiO_2 and metallic Ag or Au, respectively, during the heat treatment. For both Ag@1D-TiO_2 and Au@1D-TiO_2, the full-width half-maximum (FWHM) of TiO_2 became broader and the intensity of the TiO_2(101) peak appeared to be substantially decreased because of the incorporated metal nanoparticles. Based on these FWHM results and the angular position ($2\theta_{max}$) of the TiO_2(101) peak, the average particle size of TiO_2 was calculated by a Gaussian-fitted (101) peak according to the Scherrer model. The pristine 1D-TiO_2 was composed of nanoparticles of ca. 9 nm in diameter, which is in agreement with the individual particle size observed in TEM images. In contrast, the average particle size of the TiO_2 in Ag@1D-TiO_2 or Au@1D-TiO_2 was ca. 6 nm.

Local structural changes in the Ti states were investigated using X-ray absorption near edge structure (XANES) around the Ti K-edge (4966 eV) in a qualitative manner by comparing the shape, relative intensity, and derivative of the pre- or postedge peaks of XANES spectra with those of reference materials (30, 31). As shown in Figure 3a, all prepared materials exhibited shapes similar to the reference sample of anatase TiO_2. However, small differences between 1D-TiO_2 with and without metal nanoparticles were observed at the pre- and postedge regions. The separation of triple pre-edge peaks and the stronger multiple scattering peaks at the postedge region in the Ag@1D-TiO_2 and Au@1D-TiO_2 indicated that they are similar to the anatase phase. All inflection points of the Ag@1D-TiO_2 and Au@1D-TiO_2 were located at the same energy positions as in the anatase TiO_2. Accordingly, these results indicate that the embedded metallic nanoparticles had insignificant effects on the electronic configuration of TiO_2 despite the slightly different nanostructures of TiO_2 compared to those previously described. The Fourier transform (FT) in Figure 3b shows three shells of backscattering atoms around the central Ti atoms in the prepared 1D-TiO_2, Ag@1D-TiO_2, and Au@1D-TiO_2. Both the

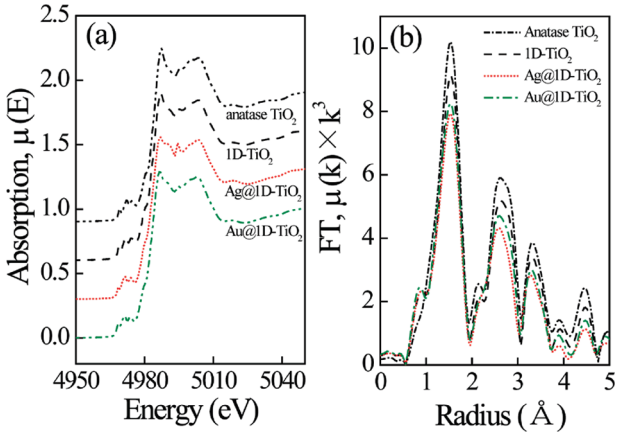

FIGURE 3. X-ray absorption spectroscopy of TiO_2 at Ti K-edge (E_0 = 4966 eV). (a) normalized X-ray absorption near edge spectrum (XANES) and (b) normalized magnitude of Fourier transforms of the transmission mode spectra of anatase TiO_2, 1D-TiO_2, Ag@1D-TiO_2, and Au@1D-TiO_2. The data are not phase-shift corrected. Kaisser-Bessel windows, k range of $2.5 \leq k \leq 12$ Å^{-1}, were used for the Fourier transform of extended X-ray absorption fine structure (EXAFS).

first (Ti—O) and second (Ti—Ti) shells in all of the FT peaks were derived from single scattering paths using FEFF 8.4 code (26) applied to a theoretical anatase TiO_2. The third FT peaks are associated with single and multiple scattering paths such as Ti—O, Ti—Ti, Ti—Ti—O, Ti—O—Ti—O, etc. The amplitudes of the FT peaks for 1D-TiO_2, Ag@1D-TiO_2, and Au@1D-TiO_2 were reduced compared to those of bulk anatase TiO_2. In addition, compared to 1D-TiO_2, further reductions of the amplitude for both Ag@1D-TiO_2 and Au@1D-TiO_2 were observed with decreasing TiO_2 particle size, suggesting that the first (Ti—O) and second (Ti—Ti) shells increased the mean square relative displacement (32).

To investigate the electrochemical properties of metallic nanoparticles embedded in 1D-TiO_2, we carried out galvanostatic cyclings. As shown in panels a and b in Figure 4, the potential window from 1.0 to 3.0 V (vs Li^+/Li) was studied at a constant current density (ca. 0.033 A g^{-1}). The specific capacities of the Au- or Ag-embedded TiO_2 nanofibers were improved by 20% or more compared to the pristine 1D-TiO_2 (Figure 4c, d). The initial Coulombic efficiencies in 1D-TiO_2 and Ag@1D-TiO_2 displayed irreversible capacities of 70 and 120 mAh g^{-1}, respectively, during the first discharge and charge process, whereas that of Au@1D-TiO_2 was ca. 20 mA h g^{-1} (Figure 4a). The irreversible capacity difference between the tested materials might be caused by changes in surface area. Au@1D-TiO_2 had a decreased surface area after Au incorporation (will be discussed later), which led to a reduced electrolyte-electrode contact area (33). In contrast, Ag@1D-TiO_2 and 1D-TiO_2 had larger irreversible capacity, implying that their surface area may be related to the irreversible capacity. Additionally, side reactions arising from trace water adsorbed on TiO_2 might be responsible for the irreversible loss (34). The plateaus around 1.9 and 1.75 V in Figure 4b are related to the reversible framework transitions for the insertion/extraction of Li-ions into the anatase TiO_2 (35). Furthermore, both Li-ion diffusion and the electronic conductivity of TiO_2 influence the span of the potential plateaus (36). Therefore, the increased potential plateau with a sluggish slope appearing for both Ag@1D-TiO_2 and Au@1D-TiO_2 suggests that the storage performance is enhanced. The generated capacity below 1.7 V is ca. 60% at a slow scan rate (at 0.033 A g^{-1}), suggesting that the surface reaction is dominant. For all prepared 1D-TiO_2, Ag@1D-TiO_2, and Au@1D-TiO_2 samples, Figure 4c shows remarkable cycling stability and reversibility, indicating that no significant structural changes occurred during the cycling. This structural maintenance of the electrode materials may be attributed to the reduced particle size of TiO_2, which may prevent fracture of TiO_2 particles with the movement of Li ions (37). The relationship between the cycling performance and the current density for the prepared samples is shown in Figure 4d. As the current density increased, the relative capacity loss of Ag@1D-TiO_2 and Au@1D-TiO_2 was less than that of pristine TiO_2. The Ag@1D-TiO_2 and Au@1D-TiO_2 exhibited exceptional rate capabilities unlike the pristine 1D-TiO_2. In particular, Au@1D-TiO_2 showed higher rate performance than the others at the increased current density. The capacity differences became remarkably higher as the c-rate was increased from 30% at 0.1 C to at least 2-fold at 2 C and 24-fold at 5 C for the Au@1D-TiO_2 compared to samples without Au incorporation. These results may be attributable to the low irreversible capacity and the more complete discharge/charge reaction of Au@1D-TiO_2. The metallic nanoparticles of Ag or Au in our work do not function as lithium host matrices because their potential window do not include any redox potential peaks corresponding to these metal components during cycling (38, 39).

Further confirmation of charge transport rates in the Ag@1D-TiO_2 and Au@1D-TiO_2 was carried out using cyclic voltammetry with varying scan rates from 0.1 to 2 mV s^{-1}. As shown in Figure 5a—c, growing peak-to-peak separations were observed as the scan rate was increased. The Ti^{4+}/Ti^{3+} redox couple, which is responsible for the electrochemical activity, was shown to occur during the discharge/charge process. Generally, because the position of the peak potential is related to the scan rate and the mass transfer rate, the systems demonstrated irreversibility at higher scan rate while moving the cathodic and anodic peaks toward lower and higher potentials, respectively. Metal incorporation can alleviate the mass transfer rate of Li ions (40). The peak separations in the Ag@1D-TiO_2 and Au@1D-TiO_2 appeared to be ca. 0.43 V, whereas the pristine sample was found to have a peak separation of ca. 0.50 V. In previous research (41), such peak separations occurred at low overpotentials, and the peak values were usually smaller for materials with large surface area than for materials with small surface areas. Therefore, we can postulate that Ag@1D-TiO_2 and Au@1D-TiO_2 (Figure 5b, c) have better reversibilities than 1D-TiO_2 along the small potential differences. These results are consistent with the structural changes (Figures 1—3), and with the Coulombic efficiencies and the cycle retention shown in Figure 4.

The Li-ion diffusion coefficient can be derived by the following peak current equation (42)

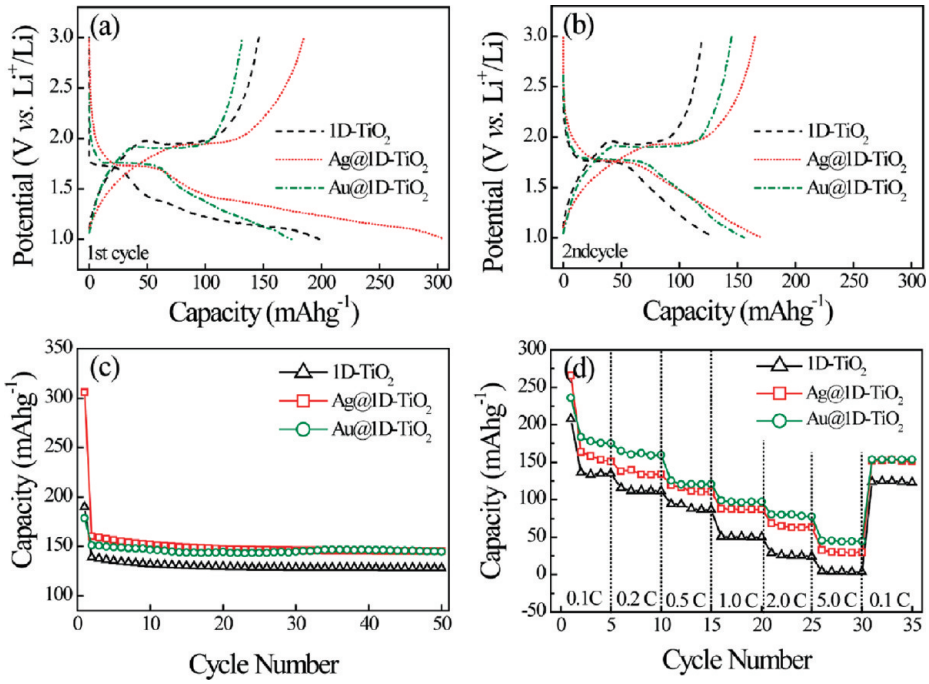

FIGURE 4. Initial galvanostatic discharge−charge profiles of (a) first cycle and (b) second cycle for the pristine 1D-TiO_2, Ag@1D-TiO_2, and Au@1D-TiO_2. (c) Cycle performance on the discharge capacities of the test cells at the constant current density. (d) Specific capacity of the prepared samples at different current density (0.033−1.65 A g^{-1}).

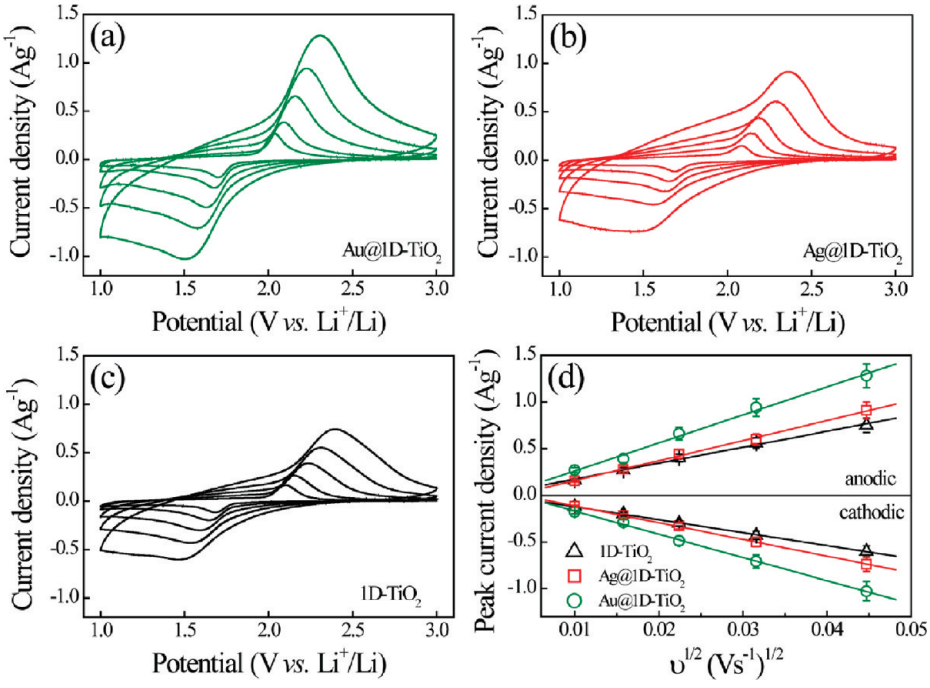

FIGURE 5. Cyclic voltammetry of (a) Au@1D-TiO_2, (b) Ag@1D-TiO_2, and (c) 1D-TiO_2 at various scan rates from 0.1 to 2 mV s^{-1}. (d) Relationship between the peak current density and the square root of scan rate.

$$I_p = (2.69 \times 10^5) n^{3/2} A D^{1/2} C_0 \upsilon^{1/2}$$

where n is the number of electrons transferred, I_p is the current density (A g^{-1}), A is the surface area of the anode (cm^2 g^{-1}), D is the diffusion coefficient of the Li ions (cm^2 s^{-1}), C_0 is the concentration of Li ions ($C_0 = 0.024$ mol cm^{-3} for $x = 0.5$) (43), and υ is the scan rate (V s^{-1}). The surface areas of 1D-TiO_2, Ag@1D-TiO_2, and Au@1D-TiO_2 were measured to be ca. 55, 53, and 25 m^2 g^{-1}, respectively, and were analyzed by N_2 adsorption/desorption isotherms (not shown here). After the metal nanoparticles were incorporated, a new pore size of ca. 3.5 nm was observed. For the relation of I_p and $\upsilon^{1/2}$ shown in Figure 5d, the Ag@1D-TiO_2 and Au@1D-TiO_2 had steeper slopes than the pristine 1D-TiO_2 sample. Au@1D-TiO_2 appeared to have a diffusion coefficient of ca. 2.8×10^{-15} cm^2 s^{-1}, which is approxi-

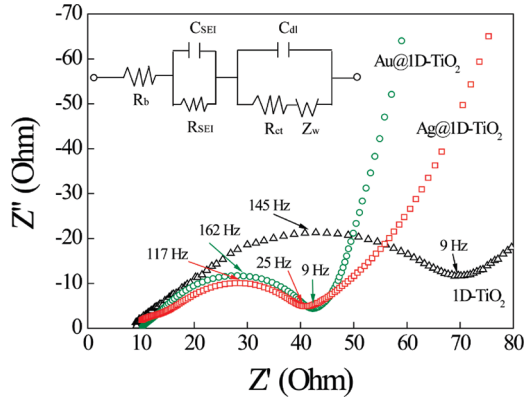

FIGURE 6. AC impedance spectra for 1D-TiO_2 (triangle), Ag@1D-TiO_2 (square), and Au@1D-TiO_2 (circle) presented as Nyquist plots, which were measured at $E = 2.5$ V (vs Li^+/Li) after cycles. The equivalent circuit for the AC impedance spectra is depicted in the inset. R_b is the electrode resistance, C_{SEI} and R_{SEI} are the capacitance and resistance of the surface film, respectively, C_{dl} and R_{ct} are the double-layer capacitance and charge-transfer resistance, respectively, and Z_W is the Warburg impedance.

mately one-order higher than that of 1D TiO_2 (ca. 2.0×10^{-16} cm^2 s^{-1}). The diffusion coefficient of Ag@1D-TiO_2 was similar to that of 1D TiO_2 with 2.8×10^{-16} cm^2 s^{-1}.

To probe the kinetic properties of Ag@1D-TiO_2 and Au@1D-TiO_2, we took AC impedance spectroscopy measurements at a potential of 2.5 V. All three plots showed partially overlapping semicircles at high-to-medium frequencies, and a line was observed at low frequencies in Figure 6. Both R_{ct} and C_{ct} in Ag@1D-TiO_2 or Au@1D-TiO_2 appeared to be smaller than those in 1D TiO_2, whereas the R_b values were similar, indicating that the electrochemical properties were improved by metal incorporation into the host 1D TiO_2 matrix materials. The interfacial resistance of the solid-state electrolyte was decreased in both Ag@1D-TiO_2 and Au@1D-TiO_2, which facilitate Li-ion diffusion. Thus, the metal-incorporated electrodes produced thin solid electrolyte interface (SEI) layer impedance, which can cause smaller cell polarization, enhanced charging and discharging property, and less capacity fading (44). Additionally, in comparison to the semicircles of 1D-TiO_2, the overall charge transfer resistances in both Ag@1D-TiO_2 and Au@1D-TiO_2 were lower. In contrast, the contact resistance (see the intercept of the real axis in Figure 6) between electrolyte and electrode materials of the metal-embedded samples were similar to those of pristine TiO_2. Therefore the metal incorporation boosted the electronic conductivity (15–17). We conclude that the high specific capacities of Ag@1D-TiO_2 and Au@1D-TiO_2 were mainly caused by the electrical conductivity, which was consistent in the comparison of the specific capacities at high scan rate in Figures 4c,d and 5d.

To elucidate the cycling stability of the Au@1D-TiO_2 samples, TEM images were examined after 50 cycles. As shown in Figure 7a, a smooth sidewall with a diameter of ca. 80 nm was typically observed in our tested samples. The cycled metal-embedded 1D TiO_2 exhibited a morphology similar to that of the synthesized 1D TiO_2. This is in contrast to the previously reported capacity decrease of TiO_2 nanoparticles, in which the lattice expanded via lithium insertion

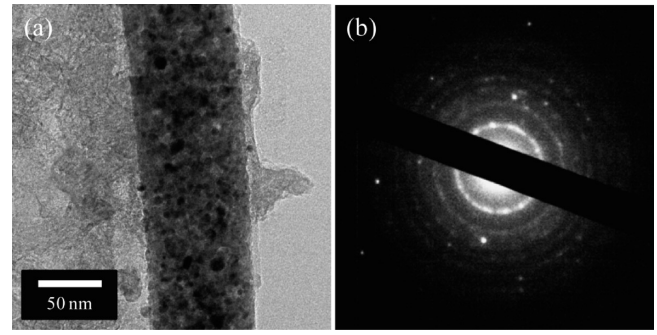

FIGURE 7. Images of (a) TEM and (b) SAED pattern after finishing the 50th galvanostatic discharge–charge cycling of Au@1D-TiO_2. The depicted transparent sheet is the acetylene black as a conducting agent.

and extraction (36). Similarly, the blurred diffuse patterns in Figure 7b are attributed to the strain from the lattice expansion. Nevertheless, it is worth noting that 1D TiO_2 nanoparticles maintain their structural integrity during the entire cycling process, which implies that no significant structural degradation of the TiO_2 nanoparticles takes place during the cycling. The SAED pattern in Figure 7b also confirms that TiO_2 still maintains its crystallinity after repeated cycling processes. The stable cycle performance might be associated with the maintained crystalline phase. The diffuse ring patterns in Figure 7b show broadened and blurred line profiles compared to those of the synthesized sample, implying that some Li ions remain in the host matrix despite the potential value specified by full extraction. Such an inability to remove all of the inserted Li has been reported in previous research (4). The 1D-TiO_2 and Ag@1D-TiO_2 showed similar structural integrity and line profiles after 50 cycles (not shown here), suggesting that the 1D nanostructures restrict the phase transition of individual TiO_2 nanoparticles during Li-ion insertion and extraction. Consequently, the 1D TiO_2 structure that consists of integrated TiO_2 nanoparticles is helpful for maintaining cycling stability.

CONCLUSIONS

We synthesized Ag@1D-TiO_2 and Au@1D-TiO_2 using a simple one-step electrospinning method. The electronic configurations were maintained even when the metallic nanoparticles (Ag or Au) were introduced into the 1D TiO_2. Importantly, the embedded Ag or Au nanoparticles were found to contribute to the nanostructures and electrochemical properties of the 1D TiO_2. The particle size of the TiO_2 consisting of the 1D nanostructure was reduced after the incorporation of Ag or Au nanoparticles into 1D TiO_2. At the same time, the inserted Ag or Au nanoparticles not only decreased the charge transfer of the composite TiO_2, but also functioned as conductive agents. Regarding Li-ion storage performance, the capacity was improved by 20% or more compared to pristine 1D TiO_2 through changes in crystallinity and charge transfer upon Ag or Au incorporation. In particular, Au@1D-TiO_2 showed higher lithium storage performance than the others. Smaller particle size and better charge transfer contributed to the improved electrochemical properties and cycling stability of Ag@1D-TiO_2 and Au@1D-

TiO_2. In contrast, Ag@1D-TiO_2 showed less significant changes than Au@1D-TiO_2 because of poor crystallinity after incorporation of Ag. Our study suggests that the controlled incorporation of metallic nanoparticles into a 1D Li host matrix may be a promising approach for realizing high-rate Li-ion storage device.

Acknowledgment. This work was supported by Basic Science Research Program through the National Research Foundation of Korea (NRF) funded by the Ministry of Education, Science and Technology (R15-2008-006-03002-0) and by the Korean government (MEST) (No.20090058918) and by the Program for Integrated Molecular Systems (PIMS/GIST). We also appreciate Dr. S. H. Choi, Dr. N. E. Sung, and Dr. M. G. Kim at the PAL for help in XAFS experiments.

REFERENCES AND NOTES

(1) Jiang, J.; Chen, J.; Dahn, J. R. *J. Electrochem. Soc.* **2004**, *15*, A2082.
(2) Hu, Y.-S.; Kienle, L.; Guo, Y.-G.; Maier, J. *Adv. Mater.* **2006**, *18*, 1421.
(3) Das, S. K.; Darmakolla, S.; Bhattacharyya, A. J. *J. Mater. Chem.* **2010**, *20*, 1600.
(4) Amstrong, G.; Amstrong, A. R.; Canales, J.; Bruce, P. G. *Electrochem. Solid-State Lett.* **2006**, *9* (3), A139.
(5) Bing, Z.; Yuan, Y.; Wang, Y.; Fu, Z.-W. *Electrochem. Solid-State Lett.* **2006**, *9* (3), A101.
(6) Poizot, P.; Laruelle, S.; Grueon, S.; Dupont, S.; Tarascon, J.-M. *Nature* **2000**, *407*, 496.
(7) Oh, S. W.; Park, S.-H.; Sun, Y.-K. *J. Power Sources* **2006**, *161*, 1314.
(8) Lee, S.-H.; Deshpande, R.; Benhammou, D.; Parilla, P. A.; Mahan, A. H.; Dillon, A. C. *Thin Solid Films* **2009**, *517*, 3591.
(9) Stashans, A.; Lunell, S.; Bergstrom, R. *Phys. Rev. B* **1996**, *53*, 159.
(10) Mizoguchi, T.; Tanaka, I.; Yoshioka, S.; Kunisu, M.; Yamamoto, T.; Ching, W. Y. *Phys. Rev. B* **2004**, *70*, 045103.
(11) Marchand, R.; Brohan, L.; Toumoux, M. *Mater. Res. Bull.* **1980**, *15*, 1129.
(12) Wang, Y.; Wu, M.; Zhang, W. F. *Electrochim. Acta* **2008**, *53*, 7863.
(13) Kang, S. H.; Choi, S.-H.; Kang, M.-S.; Kim, J.-Y.; Kim, H.-S.; Hyeon, T.; Sung, Y.-E. *Adv. Mater.* **2008**, *20*, 54.
(14) Das, S. K.; Bhattacharyya, A. J. *J. Phys. Chem. C* **2009**, *113*, 17367.
(15) Huang, S.; Wen, Z.; Yang, X.; Gua, Z.; Xu, X. *J. Power Sources* **2005**, *148*, 72.
(16) Shu, Z. X.; McMillan, R. S.; Murray, J. J. *J. Electrochem. Soc.* **1993**, *140*, 922.
(17) Yan, J.; Song, H.; Yang, S.; Chen, X. *Mater. Chem. Phys.* **2009**, *118*, 367.
(18) Kim, Y.-S.; Ahn, H.-J.; Nam, S. H.; Seong, T. Y.; Kim, W. B. *Electrochem. Solid-State Lett.* **2007**, *10* (8), A180.
(19) Nam, K. T.; Kim, D.-W.; Yoo, P. J.; Chiang, C.-Y.; Meethong, N.; Hammond, P. T.; Chiang, Y.-M.; Belcher, A. M. *Science* **2006**, *312*, 885.
(20) Yan, J.; Song, H.; Yang, S.; Yan, J.; Chen, X. *Electrochim. Acta* **2008**, *53*, 6351.
(21) Hosono, E.; Wang, Y.; Kida, N.; Enomoto, M.; Kojima, N.; Okubo, M.; Matsuda, H.; Saito, Y.; Kudo, T.; Honma, I.; Zhou, H. *ACS Appl. Mater. Interface* **2010**, *2* (1), 212.
(22) Kim, Y. S.; Nam, S. H.; Shim, H.-S.; Ahn, H.-J.; Anand, M.; Kim, W. B. *Electrochem. Commun.* **2008**, *10*, 1016.
(23) Wu, H.; Lin, D.; Zhang, R.; Pan, W. *Chem. Mater.* **2007**, *19* (8), 1895.
(24) Newville, M. *J. Synchrotron Rad.* **2001**, *8*, 322.
(25) Ravel, B.; Newville, M. *J. Synchrotron Radiat.* **2005**, *12*, 537.
(26) Ankudinov, A. L.; Nesvizhskii, A. I.; Rehr, J. J. *Phys. Rev. B* **2003**, *67*, 115120.
(27) Ravel, B. *J. Synchrotron Radiat.* **2001**, *8*, 314.
(28) Akita, T.; Tanaka, K.; Tsubota, S.; Haruta, M. *J. Electron Microsc.* **2000**, *49*, 657.
(29) Fang, H.-T.; Liu, M.; Wang, D.-W.; Sun, T.; Guan, D.-S.; Li, F.; Zhou, J.; Sham, T.-K.; Cheng, H.-M. *Nanotechnology* **2009**, *20*, 225701.
(30) Shim, H.-S.; Na, S.-I.; Nam, S. H.; Ahn, H.-J.; Kim, H. J.; Kim, D.-Y.; Kim, W. B. *Appl. Phys. Lett.* **2008**, *92*, 183107.
(31) Kim, W. B.; Choi, S. H.; Lee, J. S. *J. Phys. Chem. B* **2000**, *104*, 8670.
(32) Chen, L. X.; Rajh, T.; Wang, Z.; Thurnauer, M. C. *J. Phys. Chem. B* **1997**, *101*, 10688.
(33) Gao, X.; Zhu, H.; Pan, G.; Ye, S.; Lan, Y.; Wu, F.; Song, D. *J. Phys. Chem. B* **2004**, *108*, 2868.
(34) Ortiz, G. F.; Hanzu, I.; Djenizian, T.; Lavela, P.; Tirado, J. L.; Knauth, P. *Chem. Mater.* **2009**, *21*, 63.
(35) Krol, R. van der; Goossens, A.; Meulkenkamp, E. A. *J. Electrochem. Soc.* **1990**, *146*, 3150.
(36) Podhajecký, P.; Zabransky, Z.; Novak, P. *Electrochim. Acta* **1990**, *35*, 245.
(37) Huggins, R. A.; Nix, W. D. *Ionics* **2000**, *6*, 57.
(38) Park, C.-M.; Jung, H.; Sohn, H.-J. *Electrochem. Solid-State Lett.* **2009**, *12* (9), A171.
(39) Mui, S. C.; Trapa, P. E.; Huang, B.; Soo, P. P.; Lozow, M. I.; Wang, T. C.; Cohen, R. E.; Mansour, A. N.; Mukerjee, S.; Mayes, A. M. *J. Electrochem. Soc.* **2002**, *149* (12), A1610.
(40) Eftekhari, A. *Solid State Ionics* **2003**, *161*, 41.
(41) Krtil, P.; Fattakhova, D.; Kavan, L.; Burnside, S.; Grätzel, M. *Solid State Ionics* **2000**, *135*, 101.
(42) Bard, A. J.; Faulkner, L. R. *Electrochemical Methods: Fundamentals and Applications*, 2nd ed.; John Wiley & Sons: New York, 2001; p 231.
(43) Kavan, L.; Grätzel, M.; Gilbert, S. E.; Klemenz, C.; Scheel, H. J. *J. Am. Chem. Soc.* **1996**, *118*, 6716.
(44) He, B. I.; Dong, B.; Li, H. L. *Electrochem. Commun.* **2007**, *9*, 425.

AM100319U